

Mean–Standard Deviation Representation of Sonar Images for Echo Detection: Application to SAS Images

Frédéric Maussang, Jocelyn Chanussot, *Senior Member, IEEE*, Alain Hétet, and Maud Amate

Abstract—This paper addresses the detection of underwater mines echoes with application to synthetic aperture sonar (SAS) imaging. A detection method based on local first- and second-order statistical properties of the sonar images is proposed. It consists of mapping the data onto the mean–standard deviation plane highlighting these properties. With this representation, an adaptive thresholding of the data enables the separation of the echoes from the reverberation background. The procedure is automated using an entropy criterion (setting of a threshold). Applied on various SAS data sets containing both proud and buried mines, the proposed method positively compares to the conventional amplitude threshold detection method. The performances are evaluated by means of receiver operating characteristic (ROC) curves.

Index Terms—Mean–standard deviation representation, segmentation, sonar image processing, synthetic aperture sonar (SAS), Weibull law.

I. INTRODUCTION

DETECTION and classification of various types of underwater mines is currently a crucial strategic task [1], using 2-D or 3-D imagery [2]. Over the past decade, synthetic aperture sonar (SAS) has been increasingly used in seabed imaging [3], [4] providing high-resolution images [5]. An SAS consists of an active sonar, moving along a straight track, thus simulating a long antenna. Such a long antenna would be impossible to actually build, both for financial and for technical reasons. The image formation consists of a conventional process [6]: collection of pings are combined by delay compensation and beam-forming. However, as with any active coherent imaging system, the speckle constructs images with a strong granular aspect that can seriously handicap the interpretation of the data [7].

The literature proposes several approaches to overcome this problem [8], [9]. For instance, the speckle can be smoothed to some degree to enhance relevant features [10]. Conventional

speckle filters, such as Lee's filter [11], are based on the multiplicative property of the speckle and are derived from the synthetic aperture radar (SAR) community. Homomorphic filters [12] turn multiplicative noise into additive (thanks to the use of the logarithm function) so that common filters designed for additive noise (e.g., mean filter, median filter, etc.) may be used. Operators derived from mathematical morphology have also been successfully designed [13]. In the context of underwater mine hunting, former studies investigated image segmentation and detailed analysis of projected shadows using a Markovian model of the sonar image [14], [15]. Another strategy consists in classifying each pixel of the sonar image into three different classes: bottom reverberation, shadow, and echo [16], the segmentation of image pixels corresponding to the object echo (henceforth referred to as "echo") being conditioned by the presence of a segmented shadow in its neighborhood. After the segmentation process, some features characterizing the shadows are extracted, leading to the detection and recognition of the corresponding objects [17], [18]. Using data fusion, these characteristics can also be aggregated with other data to achieve a better classification [19], [20]. From *a priori* knowledge on the echoes and shadows shape of the sought targets, Hyland and Dobeck [21] designed a sonar target signature. After normalization and adaptive clutter filtering, the sonar image is correlated with a given model (mine size rectangular window), enhancing matching features. Mine-like pixels are detected using a Bayesian decision rule; they are grouped into objects. Finally, a neural network classifies these objects as either a mine or a nonmine.

In this paper, a new method of underwater mine echoes detection is presented. This paper proposes a statistical approach to solve this problem of detection and then we use image processing tools. Some *a priori* knowledge is then used in the algorithms proposed in this paper (approximative spatial extension in pixels of the echoes, for example) that are not restrictive in their use and their generalization.

It is based on the segmentation of the echoes using local statistical properties of sonar images, these properties being highlighted by the mean–standard deviation representation. For illustrative purpose, the flowchart presented in Fig. 1 schematically summarizes the proposed algorithm. In the first step, the original sonar image [Fig. 1(a)] is projected in the mean–standard deviation plane [Fig. 1(c)]. Simultaneously, the parameters of a statistical model of the sonar data are estimated [Fig. 1(b)]. From this model, the proportionality coefficient linking the mean and the standard deviation is estimated. It is

Manuscript received July 27, 2004; revised May 24, 2007; accepted September 6, 2007.

Associate Editor: R. Garello.

F. Maussang is with the Applied Electromagnetism Group (GEA), University of Paris X, 92410 Ville d'Avray, France (e-mail: frederic.maussang@u-paris10.fr).

J. Chanussot is with the GIPSA Lab, Signals and Images Department, INP Grenoble, ENSIEG, 38402 Saint-Martin-d'Hères Cedex, France (e-mail: jocelyn.chanussot@gipsa-lab.inpg.fr).

A. Hétet and M. Amate are with the Groupe d'Etudes Sous-Marines de l'Atlantique, DGA/DET/GESMA, 29240 Brest Armées, France (e-mail: alain.hetet@dga.defense.gouv.fr; maud.amate@dga.defense.gouv.fr).

Digital Object Identifier 10.1109/JOE.2007.907936

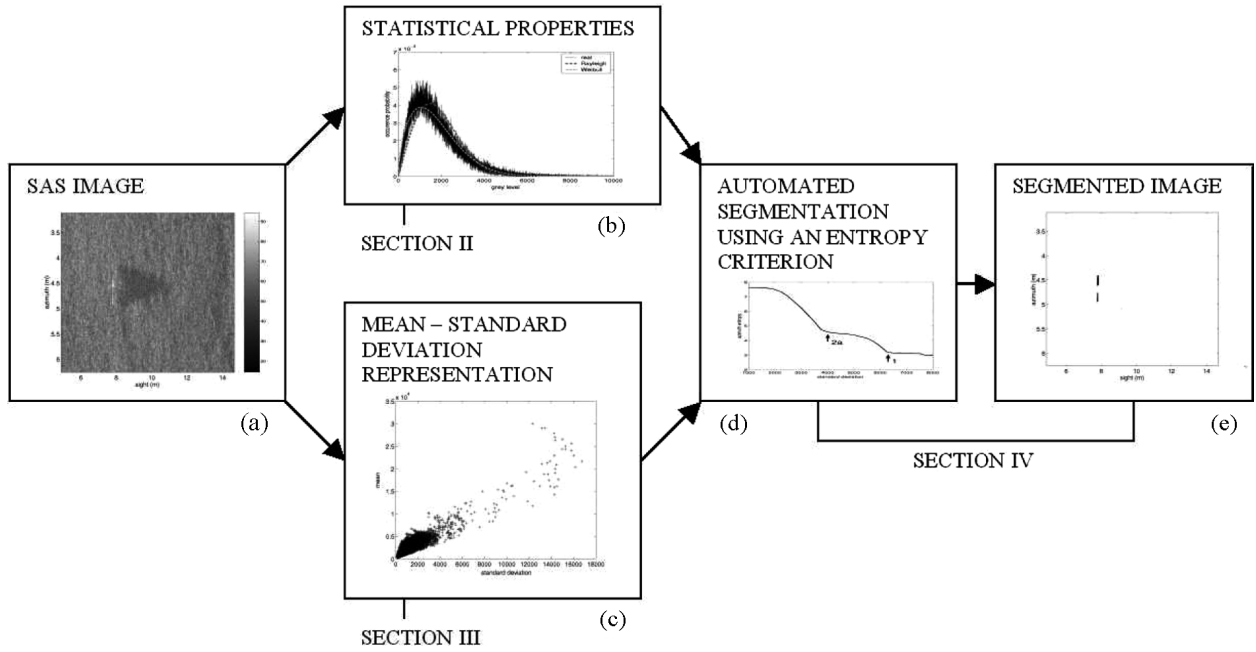


Fig. 1. Schematic flowchart of the proposed detection method: (a) original SAS image, (b) statistical model of the data (this is described in Section II), (c) mean–standard deviation representation of the data (this is described in Section III), (d and e) thresholding in the mean–standard deviation plane to segment the echoes. The thresholds are set automatically using an entropy criterion and the link between the threshold in mean and the threshold in standard deviation is derived from the statistical study (this is described in Section IV).

used to derive a mean threshold from any standard deviation threshold set. The setting of the standard deviation threshold is automated using an entropy criterion [Fig. 1(d)]. Finally, the segmented image [Fig. 1(e)] is obtained after the application of these thresholds in the mean–standard deviation representation. One should underline that, unlike most algorithms proposed in the literature, the presented method is only based on echo detection and thus remains valid in the case of sonar images with buried objects. Such images may actually not feature any cast shadow but only echoes reflected by the objects. Echoes are usually constituted of a few high-amplitude pixels. As a consequence, we will use the following model: echoes will be considered as deterministic elements surrounded by a noisy background. The size of these elements depends on the resolution in pixels and on the design of the preprocessing chain (accuracy of the delay compensation, etc.), but it is typically from 5 to 15 pixels in each direction. This parameter will be taken into account when building the mean–standard deviation representation.

This paper is organized as follows. In Section II, global and local statistical descriptions of the SAS images are presented. In Section III, the principle, the properties, and the utility of the mean–standard deviation representation used for SAS data are discussed. Finally, a segmentation method using this representation and an entropy criterion is proposed in Section IV. It is tested on several real SAS data containing both underwater mines lying on the seabed and buried objects.

To illustrate the proposed detection method, a sonar data set with a high signal-to-noise ratio (SNR; about 25 dB) is first considered. The data have been recorded on a field test during the InterFerometric Synthetic Aperture Sonar (IFSAS'99) experiment in a collaboration between the Délégation Générale pour

l'Armement (DGA, Brest, France) and the Defense Evaluation and Research Agency (DERA, Bingley, United Kingdom) [22]. The transmitter is centered on 150 kHz with a 60-kHz bandwidth (at 3 dB), moving along a straight rail. The receiver is located at the same place as the transmitter. The antenna is composed of 64 elements equally distributed at $\lambda/2$ on four different modules. Fig. 2 presents a part of the image obtained during this experiment. It represents a $3.5 \times 10\text{-m}^2$ region, with a size of a pixel of approximately 1 cm in both directions. This image contains an underwater mine lying on the seabed casting a triangular shadow on the floor. It also features echoes reflected by the object (see the specular reflections in front of the shadow). The granular texture of the image due to the speckle is clearly noticeable. Note that other more complex data sets are used to highlight the relevance of the proposed detection method in Section IV.

Also note that, for a better visualization, all the images are represented with a decibels scale. However, the algorithms described in this paper are applied to the natural values.

II. STATISTICAL DESCRIPTION OF THE SONAR IMAGES

A. Speckle Noise and the Rayleigh Law

Sonar images provided by the sonar system are constructed by the speckle. This bottom reverberation comes from the presence of a large number of elements (sand, gravel, etc.) that are smaller than the wavelength of the used monochromatic and coherent illumination source. These elements are assumed to be randomly distributed on the seabed. As a consequence, the sensor records the result of the constructive and destructive interferences of all the waves reflected by these elementary scatterers contained in a resolution cell [14], [23].

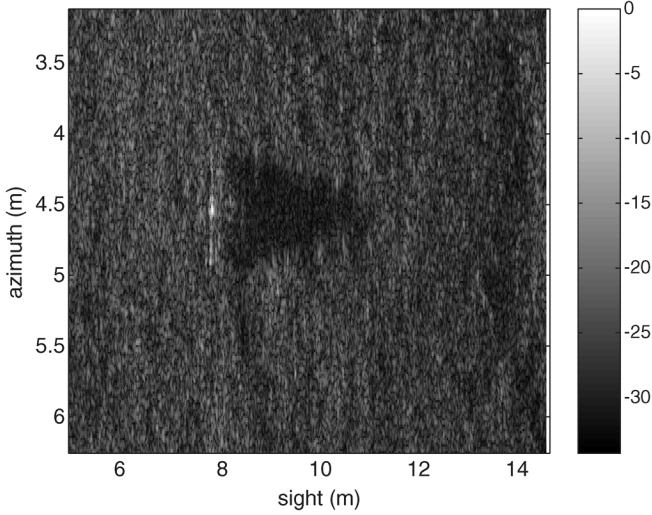


Fig. 2. Original SAS image containing a mine lying on the seabed (decibel scale, pixel size: 1 cm \times 1 cm; resolution: 2 cm \times 2 cm; antenna length: 24 cm).

The response ρ of a resolution cell can thus be described by the following:

$$\rho = \sum_{i=1}^{N_d} a_i \exp(j\varphi_i) = A \exp(j\phi) = X + jY \quad (1)$$

with A being the amplitude of the response on a resolution cell and ϕ representing the phase. The phases φ_i are usually considered as independent and uniformly distributed over $]-\pi, +\pi]$. With these assumptions, and if the number of elementary scatterers N_d within the resolution cell is large enough, the central limit theorem applies: X and Y can be considered as Gaussian random values. Consequently, the probability density function of amplitude $A = \sqrt{X^2 + Y^2}$ follows a Rayleigh distribution

$$\mathcal{R}_A(A) = \frac{A}{\alpha^2} \exp\left(-\frac{A^2}{2\alpha^2}\right), \quad A \geq 0 \quad (2)$$

with α being the Rayleigh's law specific parameter. This parameter is bound with the average intensity of the reflected waves.

The ν th-order moment of A is given by the following:

$$E(A^\nu) = (2\alpha^2)^{\nu/2} \Gamma\left(1 + \frac{\nu}{2}\right) \quad (3)$$

with Γ being the Gamma function ($\Gamma(z+1) = z! = \int_0^{+\infty} e^{-t} t^z dt$). This results in an interesting property of the Rayleigh law: the standard deviation σ_A and the mean μ_A of the amplitude A are linked by a simple proportionality relation

$$\mu_A = k_R \sigma_A \quad \text{with} \quad k_R = \sqrt{\frac{\pi}{4-\pi}} \approx 1.91. \quad (4)$$

This property leads to modeling the speckle as a multiplicative noise. As a matter of fact, the variation of amplitude induced by the speckle and characterized by parameter σ_B is bound by the mean amplitude (μ_B) with a multiplicative coefficient k_R .

B. Non-Rayleigh Models

The previous description of the speckle is the most usual and the most popular one. However, it is not satisfactory when the number of scatterers within a resolution cell (noted N_d in the previous paragraph) significantly decreases. The central limit theorem does not hold and the Rayleigh approximation is no longer valid. This case is frequently observed in high-resolution images [14], [16] such as SAS images. In this case, the amplitude A is better described by a Weibull law

$$\mathcal{W}_A(A) = \frac{\delta}{\beta} \left(\frac{A}{\beta}\right)^{\delta-1} \exp\left\{-\left(\frac{A}{\beta}\right)^\delta\right\}, \quad A \geq 0 \quad (5)$$

with β being the scale parameter and δ representing the shape parameter, strictly positive. These two parameters provide an increased flexibility compared to the Rayleigh law. Note that this law is a simple generalization of the Rayleigh distribution (in the special case $\beta = \sqrt{2}\alpha$ and $\delta = 2$, the Weibull law turns to a simple Rayleigh law).

For a Weibull distribution, the ν th-order moment of A is given by

$$E(A^\nu) = \beta^\nu \Gamma\left(1 + \frac{\nu}{\delta}\right). \quad (6)$$

Therefore, the proportionality between σ_A and μ_A still holds, but with a coefficient $k_W(\delta)$ function of δ

$$k_W(\delta) = \frac{\Gamma(1 + 1/\delta)}{\sqrt{\Gamma(1 + 2/\delta) - \Gamma(1 + 1/\delta)^2}}. \quad (7)$$

Note that for $\delta = 2$, corresponding to the Rayleigh law, we obtain the same coefficient as in (4).

Other more complex non-Rayleigh approaches have been proposed in the literature to statistically describe the bottom reverberation in high-resolution sonar imaging. One of the most famous models is the K -distribution. For this model, the number of scatterers in a resolution cell N_d is supposed to be a random variable following a negative binomial distribution. The amplitude A is then described by a K -law (called generalized K -distribution), a three parameters distribution function given by [24]

$$\mathcal{K}_A(A) = \frac{4}{\Gamma(\nu_0)\Gamma(\nu_1)} \sqrt{\frac{\nu_0\nu_1}{\mu}} \left(\sqrt{\frac{\nu_0\nu_1}{\mu}} A\right)^{\nu_0+\nu_1-1} \dots K_{\nu_1-\nu_0}\left(2\sqrt{\frac{\nu_0\nu_1}{\mu}} A\right), \quad A \geq 0 \quad (8)$$

where ν_1 is the shape parameter, μ is the scale parameter, and ν_0 is the parameter bound to the number of raw data averaged to figure out the pixel reflectivity. $K_{\nu_1-\nu_0}$ is the modified Bessel function of the second kind and order $\nu_1 - \nu_0$. This distribution describes a rapidly fluctuating Rayleigh component modulated by a slowly varying χ^2 component.

The ν th-order moment of A is then given by

$$E(A^\nu) = \left(\frac{\mu}{\nu_0\nu_1}\right)^{\frac{\nu}{2}} \frac{\Gamma(\nu_0 + \nu/2)\Gamma(\nu_1 + \nu/2)}{\Gamma(\nu_0)\Gamma(\nu_1)}. \quad (9)$$

The relationship between σ_A and μ_A is preserved, with a coefficient depending on the two parameters L and N

$$k_K(\nu_0, \nu_1) = \frac{\Gamma(\nu_0 + 1/2)\Gamma(\nu_1 + 1/2)}{\sqrt{\nu_0\nu_1\Gamma(\nu_0)^2\Gamma(\nu_1)^2 - \Gamma(\nu_0 + 1/2)^2\Gamma(\nu_1 + 1/2)^2}}. \quad (10)$$

A Rayleigh mixture has been also proposed to describe SAS data, each scattering material within a resolution cell being characterized by one specific Rayleigh distribution [25].

C. Application to Experimental Data

In this section, the performances of the different statistical models are compared using the SAS data presented in Section I (Fig. 2). For this purpose, two tests are considered: the χ^2 criterion and the Kolmogorov distance [16]. The χ^2 criterion d_{χ^2} is estimated according to the following relation [26]:

$$d_{\chi^2} = \sum_{i=1}^r \frac{(k_i - nP_i)^2}{nP_i} \quad (11)$$

where k_i is the number of realizations (number of pixels having the value i), P_i is the estimated probability of value i , r is the number of possible values, and n is the number of observations (in our case, the number of pixels).

With k'_i being the number of realizations from 1 to i and p'_i being the value for i of the cumulative distribution function associated with p_i , the Kolmogorov distance is defined as

$$d_K = \max_{i=1 \dots r} |k'_i - np'_i|. \quad (12)$$

The parameters of the Rayleigh and the Weibull laws are evaluated on the SAS image using a maximum-likelihood (ML) estimator. The estimated parameter $\hat{\alpha}_{ML}$ of the Rayleigh law (2) is given by the following [23]:

$$\hat{\alpha}_{ML}^2 = \frac{1}{2n} \sum_{i=1}^n y_i^2 \quad (13)$$

where n is the number of pixels and y_i is the amplitude of pixel i .

Parameters β and δ of the Weibull law (5) are estimated by $\hat{\beta}_{ML}$ and $\hat{\delta}_{ML}$, respectively, given by the following [16]:

$$\hat{\delta}_{ML} = \lim_{k \rightarrow +\infty} \delta_k \quad (14)$$

$$\hat{\beta}_{ML} = \left(\frac{1}{n} \sum_{i=1}^n y_i^{\hat{\delta}_{ML}} \right)^{1/\hat{\delta}_{ML}} \quad (15)$$

with $\delta_k = F(\delta_{k-1})$, $\delta_0 = 1$ (exponential law), and

$$F(x) = \frac{n \sum_{i=1}^n y_i^x}{n \sum_{i=1}^n (y_i^x \ln y_i) - \sum_{i=1}^n \ln y_i \sum_{i=1}^n y_i^x}. \quad (16)$$

These estimators are unbiased, consistent, and efficient [14].

The estimation of the K -law parameters is more problematic. Actually, there is no analytic expression for the derivative of a modified second kind Bessel function. Consequently, no ML

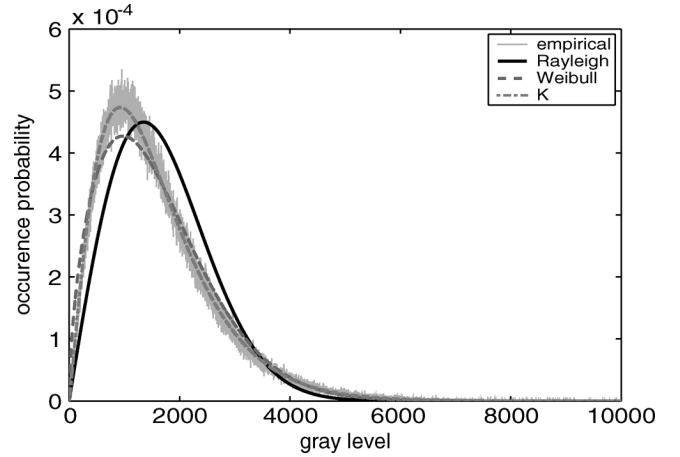


Fig. 3. Rayleigh distribution, Weibull distribution, and K -distribution estimated on the gray levels distribution (image of Fig. 2).

TABLE I
COMPARISON OF THE PERFORMANCES OF THE DISTRIBUTIONS
ON THE SAS IMAGE OF FIG. 2

Distribution	Estimated parameters	Criteria	
		χ^2	Kolmogorov
Rayleigh	$\hat{\alpha}_{ML} \approx 1482.5$	357.9	2.22×10^{-4}
Weibull	$\hat{\beta}_{ML} \approx 1961.7$ $\hat{\delta}_{ML} \approx 1.604$ (50 iterations)	0.318	1.66×10^{-4}
K	$\hat{\mu} \approx 4.300 \times 10^6$ $\hat{\nu}_0 \approx 0.882$ $\hat{\nu}_1 \approx 3.163$	0.044	1.41×10^{-4}

estimation can be performed without approximations [27]. A moments method can then be used (9), even though it does not offer a closed-form solution.

These estimators are tested on the image presented in Section I (Fig. 2). Fig. 3 presents in solid line the observed distribution (normalized histogram of the image) and compares it with the estimated Rayleigh and Weibull distributions (dashed lines). With a simple visual inspection, one immediately notices that the Weibull distribution and K -distribution fit the observed one better than the Rayleigh distribution.¹ This confirms the nonvalidity of the central limit theorem in the case of high-resolution images obtained in SAS imaging. This Rayleigh model will not be used subsequently. It is nevertheless included in this paper since the reader dealing with low-resolution sonar images may use the very same detection method proposed in this paper using the Rayleigh distribution. The K -distribution seems to provide a better statistical model of the background than the Weibull law. It especially fits better the “head” of the observed distribution. This is confirmed by the quantitative evaluation presented in Table I. However, the “tail” of the distribution is accurately estimated by both models.

¹In Fig. 2, a shadow can be seen behind the echoes reflected by the mine. Shadows are present on most sonar images containing underwater mines lying on the seabed. The shadow corresponds to a nonilluminated region of the seabed and the sensor receives a weak acoustic wave from this region: the signal related to the shadow area essentially consists of the electronic noise from the processing chain. It can also come from the “differential shadow effect” due to the variation of the shadow zone position during the imaging process. The amplitude A of the pixels in this region can thus also be modeled by a Gaussian distribution and the models remain valid.

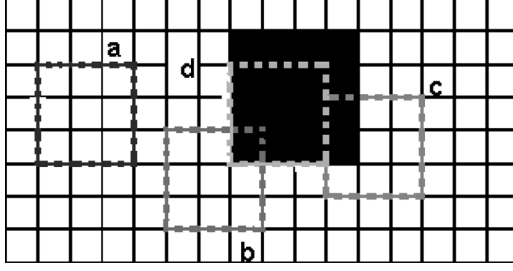


Fig. 4. Modeled echo and various values of the parameter p : (a) $p = 0$, (b) $p = 1/9$, (c) $p = 2/9$, and (d) $p = 1$.

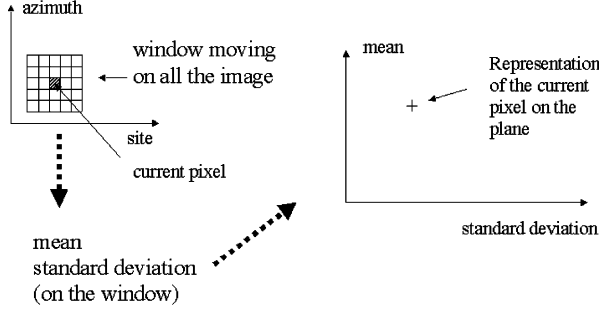


Fig. 5. Building of the mean-standard deviation representation.

D. Choice of the Statistical Model

Considering the previous remarks, the K -distribution seems to be a better model than the Weibull model. However, as we have seen in Section II-C, the estimation of K -law parameters is more difficult (no ML estimators). The estimators of the K -parameters are not optimal and the estimation takes more time. The difference with the Weibull model is not enough to justify this difficulty. Moreover, Weibull law is largely used in the sonar community and it made its proofs in their applications. That is why we will use the Weibull model in the following, but we keep in mind the existence of other models such as K .

E. Local Statistical Description

In the previous section, a global statistical description of the SAS images has been given, ignoring the presence of any echoes. This is fair since the number of target pixels in the image is too small to significantly modify the global statistics. The observed histogram matches indeed very well a Weibull law. In this section, we study local first- and second-order statistical properties. This is achieved by looking at the data through a small sliding window composed of few pixels. In this case, the potential presence of echoes can no longer be ignored.

Each echo is modeled as a deterministic element with an amplitude D surrounded by a noisy background with a Weibull distribution. We assume that the noise correlation is smaller than the spatial extension of the target echo and that the amplitude fluctuation of the echo is negligible. This is consistent with the experiments where the echoes appear as small sets of connected pixels with an almost constant value. This is justified in Fig. 6(b) with the pixels corresponding to echoes fitting the predicted ellipse in the mean-standard deviation plane.

We note p the proportion of deterministic pixels (i.e., pixels belonging to an echo) and $(1 - p)$ the proportion of random values (i.e., pixels belonging to the background) within a small square window (Fig. 4). Considering $\mu'_{D(r)}$, $\mu'_{N(r)}$, and $\mu'_{W(r)}$, the r th-order noncentral moments computed on the “echo part” of the window, the “background part” of the window, and the whole window, respectively, the following relation holds:

$$\mu'_{W(r)} = p\mu'_{D(r)} + (1 - p)\mu'_{N(r)}. \quad (17)$$

Considering $\mu_X = \mu'_{X(1)}$ and $\sigma_X^2 = \mu'_{X(2)} - \mu'^2_{X(1)}$, the mean and the variance of X , respectively [X can be replaced by D , N , or W , as in (17)], we have

$$\mu_W = p\mu_D + (1 - p)\mu_N \quad (18)$$

$$\sigma_W^2 = p(\sigma_D^2 + \mu_D^2) + (1 - p)(\sigma_N^2 + \mu_N^2) - \mu_W^2. \quad (19)$$

Moreover, echoes are considered as deterministic elements with an amplitude D , leading to

$$\mu'_{D(r)} = D^r \quad (20)$$

and

$$\mu_D = D \quad \text{and} \quad \sigma_D = 0 \quad (21)$$

and, consequently

$$\mu_W = \mu_N + p(D - \mu_N) \quad (22)$$

$$\sigma_W^2 = \sigma_N^2 + \mu_N^2 - \mu_W^2 + p(D^2 - \sigma_N^2 - \mu_N^2). \quad (23)$$

By combining (22) and (23), we obtain an interesting relationship between σ_W and μ_W

$$\sigma_W^2 + \mu_W^2 = (D + \mu_N - \lambda_{\sigma_N})\mu_W + (\lambda_{\sigma_N} - \mu_N)D \quad (24)$$

with $\lambda_{\sigma_N} = \sigma_N^2/(D - \mu_N)$. It is important to underline that this relation is independent of p . Also note that in limit cases, this relation remains valid: in the case of $p = 0$ (the window contains only background pixels), $\mu_W = \mu_N$ and $\sigma_W = \sigma_N$; in the case of $p = 1$ (the echo is filling the whole window), $\mu_W = D$ and $\sigma_W = 0$, which is consistent with (21). Remember that intermediate values of p correspond to windows being partially composed of echo pixels.

III. MEAN-STANDARD DEVIATION REPRESENTATION

A. Mean-Standard Deviation Representation

Recent studies [28], [29] proved the relevance of the projection of sonar data on the mean-standard deviation plane. Inspired by a segmentation tool applied to spectrograms [30], this enables the separation of the echoes from the bottom reverberation, both features having different statistical characteristics as stated in Section II. In [31], the link between first- and second-order statistics is highlighted using this representation.

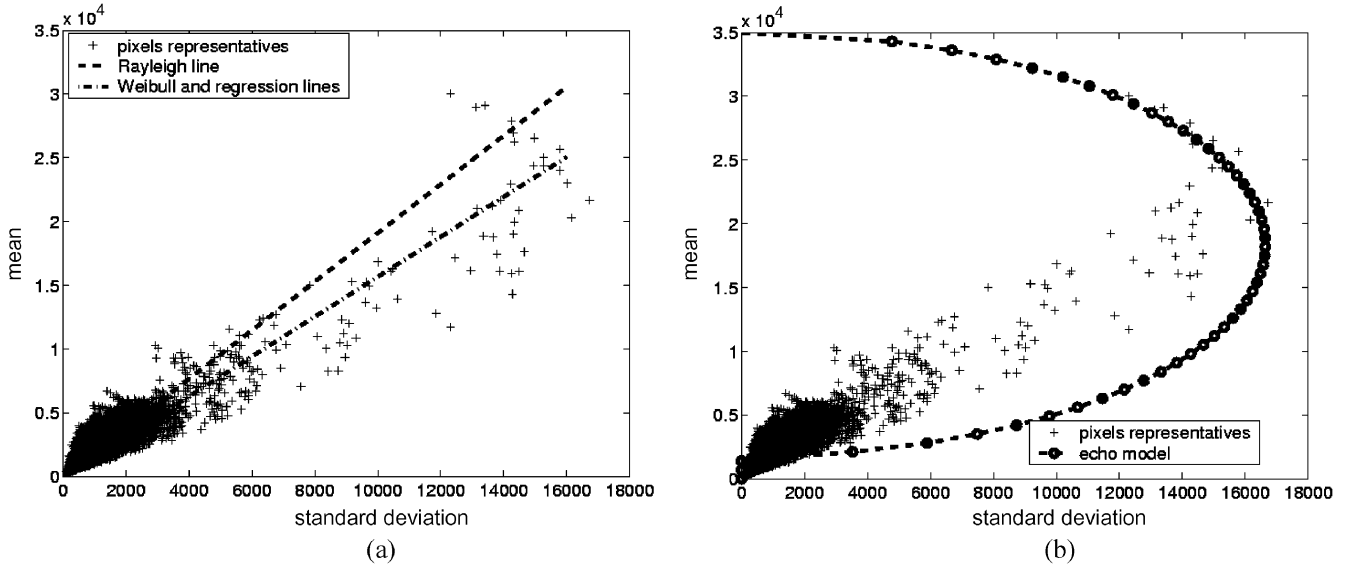


Fig. 6. Mean-standard deviation representation of the SAS image (5 cm \times 5-cm window). The linear approximations are estimated by the Rayleigh law, the Weibull law, and a regression. (a) Linear approximations. (b) Echo model.

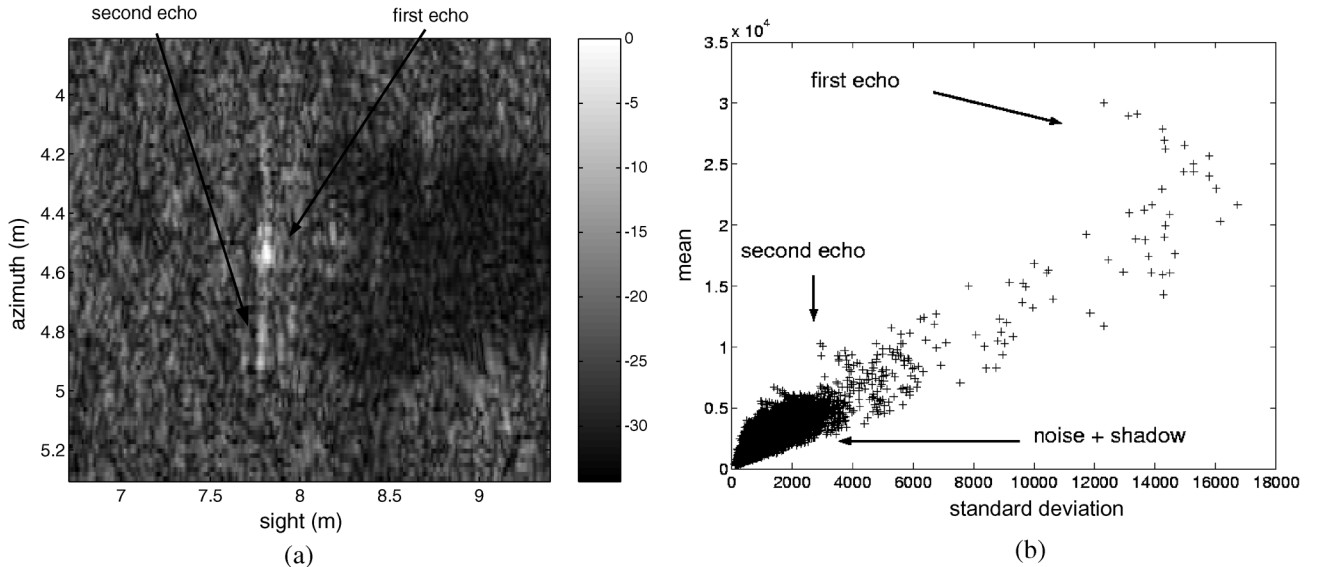


Fig. 7. Comparison between the SAS image (Fig. 2) and its mean-standard deviation representation. (a) Zoom of the SAS image. (b) Representation.

Whereas in [31] this link is simply illustrated as a justification to use first- and second-order statistics, the method proposed in this paper actually performs a segmentation of the mean-standard deviation plane.

The idea is to change the representation space of the data to highlight local statistical properties. The chosen space is the mean-standard deviation plane. For each pixel, the local standard deviation $\hat{\sigma}_W$ and the local mean $\hat{\mu}_W$ are estimated within a square-centered computation window with the following conventional equations:

$$\hat{\mu}_W = \frac{1}{N} \sum_{i=1}^N y_i \quad (25)$$

$$\hat{\sigma}_W = \sqrt{\frac{1}{N} \sum_{i=1}^N (y_i - \hat{\mu}_W)^2} \quad (26)$$

where N is the number of pixels in the computation window ($N = N_x \cdot N_y$ with N_x and N_y being the length and the width

of the window, respectively) and y_i is the value of pixel i in the window. The pair $(\hat{\sigma}_W, \hat{\mu}_W)$ becomes the coordinates representing the current pixel in the mean-standard deviation plane (Fig. 5). The performances of these estimators are evaluated by computing their moments [30]. For the mean estimator $\hat{\mu}_W$, the mean $\mathcal{M}(\hat{\mu}_W)$ and the variance $\mathcal{V}(\hat{\mu}_W)$ are

$$\mathcal{M}(\hat{\mu}_W) = \mu_W \quad (27)$$

$$\mathcal{V}(\hat{\mu}_W) = \frac{\sigma_W^2}{N}. \quad (28)$$

The mean estimator is unbiased and consistent with a variance varying as $1/N$. For the standard deviation estimator, the mean $\mathcal{M}(\hat{\sigma}_W)$ and the variance $\mathcal{V}(\hat{\sigma}_W)$ are given by

$$\mathcal{M}(\hat{\sigma}_W) \approx \frac{1}{2N} \frac{\sqrt{(4N^2 - 3N - 3)\sigma_W^4 - (N-1)m_{W(4)}}}{\sigma_W} \quad (29)$$

$$\mathcal{V}(\hat{\sigma}_W) \approx \frac{1}{4N^2} \frac{(N-1)m_{W(4)} - (N-3)\sigma_W^4}{\sigma_W^2} \quad (30)$$

with $m_{W(4)}$ being the fourth central moment computed on the window. These equations come from the approximation $\mathcal{V}(\sqrt{X}) \approx \mathcal{V}(X)/4\mathcal{M}(X)$ with X being a random variable [32]. This estimator is asymptotically unbiased and is consistent with a variance varying as $1/N$.

The choice of the size of the computation window is a tradeoff. On one hand, the variance of the estimators [see (25) and (26)] increases for small values of N . N should thus not be too small to enable an accurate estimation. On the other hand, if N is too high, echoes being small elements, the proportion of the deterministic elements p in the computation windows remains low and echoes are lost in the background speckle [see (24)]. Consequently, the computation window should be chosen as slightly larger than the spatial extension of the echoes, this size depending on the resolution of the sonar image and the quality of the preprocessing chain.

B. Observations on the Representation

The mean–standard deviation representation of Fig. 2 image is built with a 5×5 -cm² window and is presented in Fig. 6. A general linear orientation is observed, as well as some pixels distancing the main direction on the right [see Fig. 6(b)].

Three different linear regressions of the data in the mean–standard deviation plane can be computed. They are shown in Fig. 6(a). The first line, with a slope of approximately 1.91, corresponds to the proportionality relation between the mean and the standard deviation estimated when assuming that the bottom reverberation is modeled by a Rayleigh law (4). The second line, with a slope of approximately 1.57, corresponds to the proportionality relation estimated with a Weibull model (7). At the given computation accuracy (10^{-2}), the same line is obtained by a linear regression using a mean square method on the pixels representatives. To describe the global linear orientation of the data in the mean–standard deviation plane, the proportionality coefficient estimated with the Weibull assumption clearly outperforms the estimation based on a Rayleigh law. This confirms the previous results for the case of high-resolution data (Table I).

In Fig. 6(b), the curve corresponding to the local relationship between mean–standard deviation on a computation window (24) is plotted considering a deterministic element with an amplitude of $D = 3.4 \times 10^{-4}$, approximately corresponding to the typical amplitude of the main echo on the original SAS image. This curve is a part of an ellipse and is a fairly good estimation of the main structure. See Fig. 16(a) for other examples. Results obtained on other data sets could not be presented in this paper for confidentiality reasons. We will see in Section III-C that each structure can be associated with one echo on the SAS image.

The fact that no pixels are on the Y-axis of this representation comes from the size of the computation window sensibly larger than the echoes. Therefore, no window contains only echo pixels and all the windows have a part of background. Moreover, the hypothesis of a constant deterministic echo is not strictly valid, the pixels of one echo having different, but similar, values. However, the value of our model is not called into question to explain the results described previously.

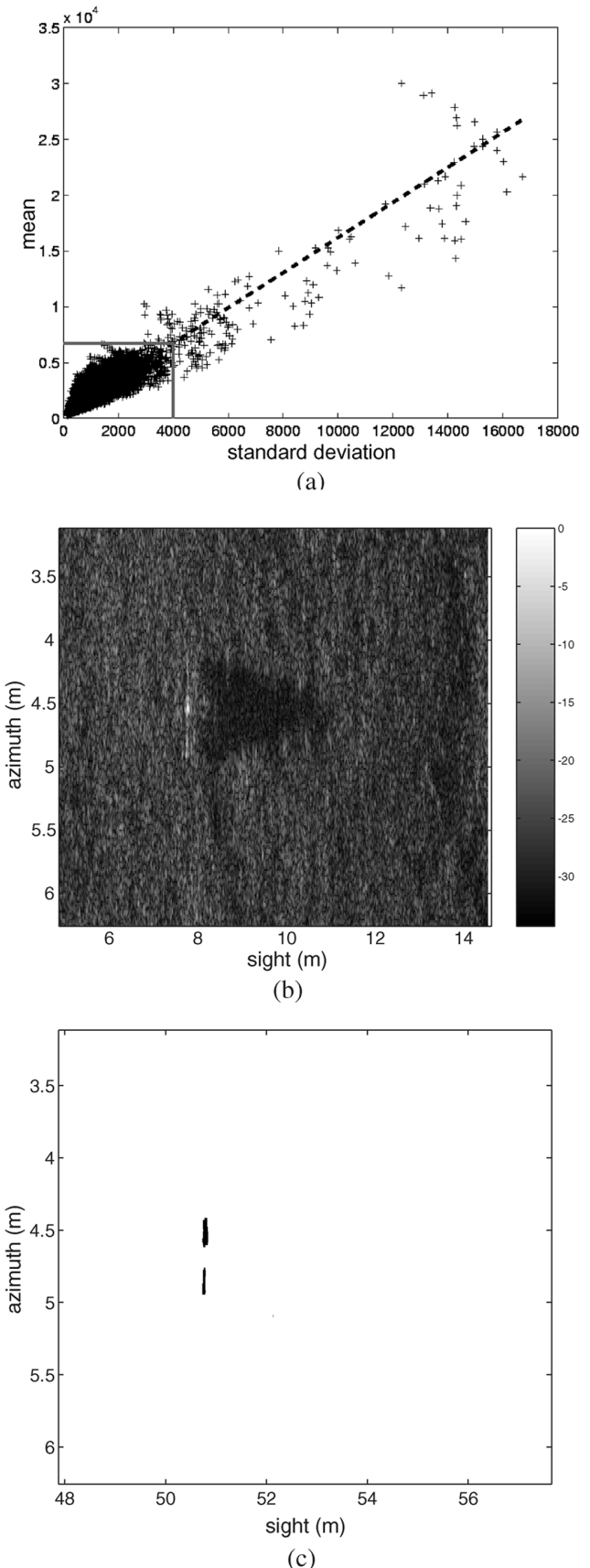
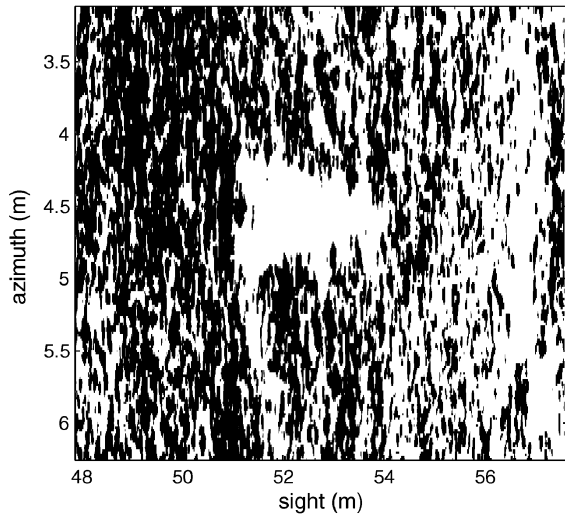
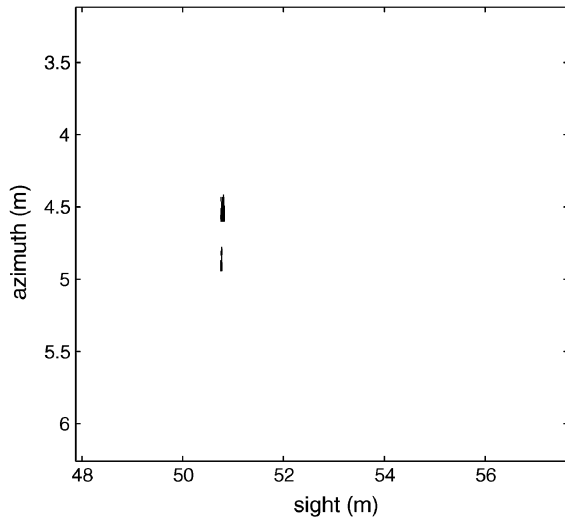


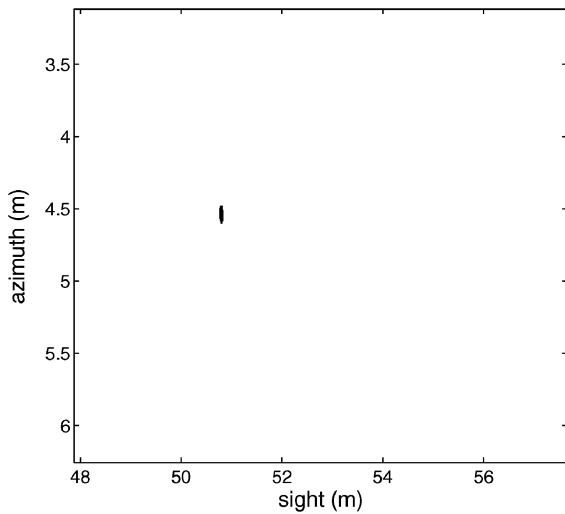
Fig. 8. Segmentation of the SAS image of Fig. 2 (thresholds: standard deviation: 4000; mean: 6751). (a) Thresholds (in thick lines). (b) SAS image. (c) Result of the segmentation.



(a)



(b)



(c)

Fig. 9. Segmentation results for different thresholds in standard deviation. (a) Threshold 1000. (b) Threshold 5000. (c) Threshold 8000.

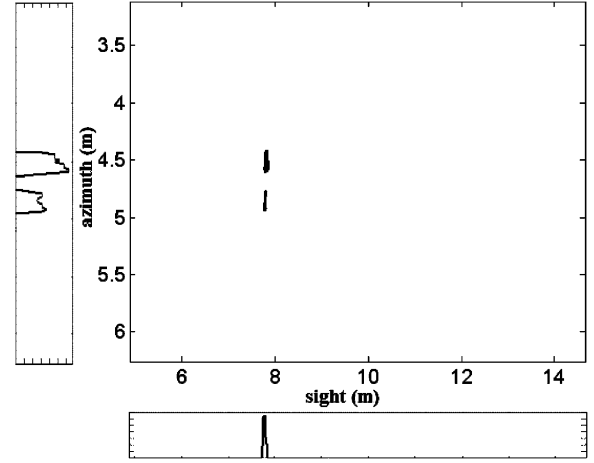


Fig. 10. Segmented SAS image and repartition of the segmented pixels according to the two axes. Computed entropies: X -axis: 3.46; Y -axis: 4.58.

C. Relationships Between the Mean-Standard Deviation Representation and the Sonar Image

To highlight interesting properties of the mean-standard deviation representation, it is compared with the original image. Fig. 7 presents a zoom of the original image featuring two mine echoes and the corresponding mean-standard deviation representation.

For a better understanding, a manual labeling of the sonar image is performed: pixels corresponding to the echoes are selected and corresponding points on the mean-standard deviation representation can be inspected. It turns out that the cluster of points close to the origin of the mean-standard deviation plane corresponds to the bottom reverberation pixels on the SAS image, with low means and low standard deviations. On the contrary, horn-shaped structures (actually parts of ellipses) correspond to the echoes on the sonar image. Two main structures can be seen with different positions and dimensions, each one corresponding to one specific echo. The extremities of these structures correspond to the centers of the echoes which are deterministic elements (high mean and relatively low standard deviation). The intermediary points correspond to the transition between echoes and background (increasing standard deviation and decreasing mean). These properties can be used to classify the different elements on the sonar image by observing the mean-standard deviation plane and the characteristics of the different structures.

IV. SEGMENTATION

A. Description of the Segmentation Method

Based on the statistical study and the observations previously presented, we propose in this section a segmentation method. The aim is to design an automatic algorithm isolating the echoes from the reverberation background on the sonar images. The proposed method is decomposed into the following steps.

- The Weibull distribution best fitting the observed normalized histogram is estimated with an ML estimator.

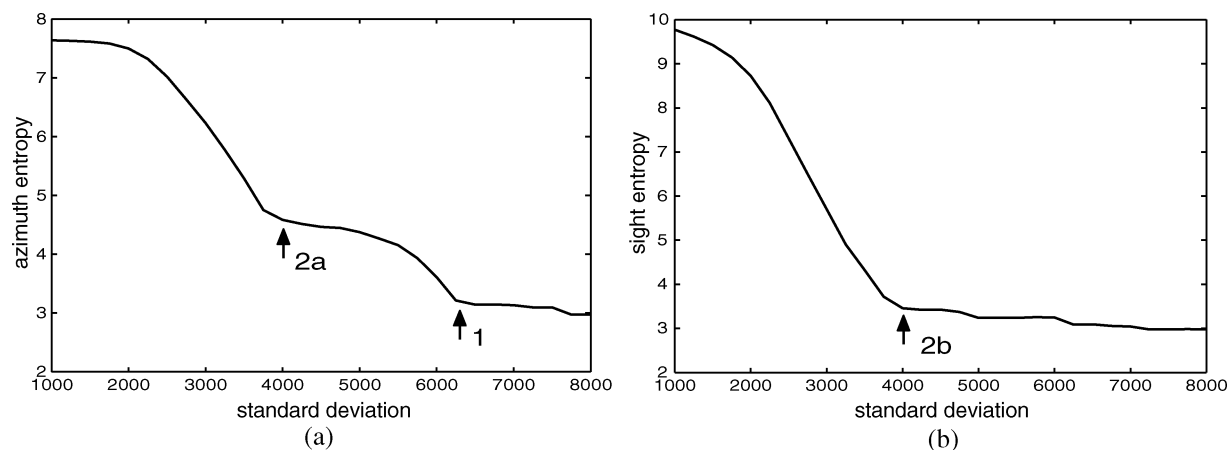


Fig. 11. Entropy variation on the two axes in function of the threshold in standard deviation. (a) Azimuth axis. (b) Sight axis.

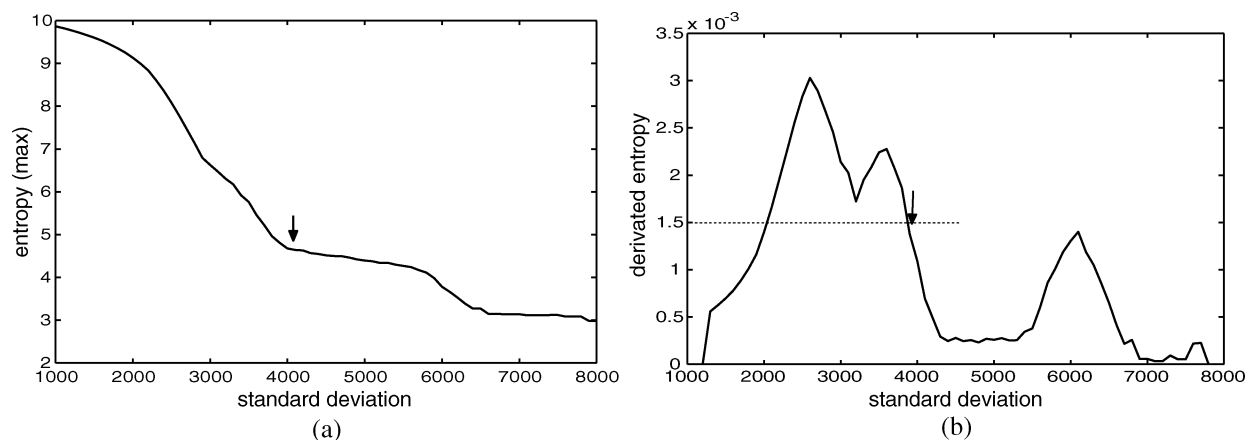


Fig. 12. Maximum of the entropies, its derivative, and setting of the threshold (see the arrows). (a) Entropy (max). (b) Derived entropy.

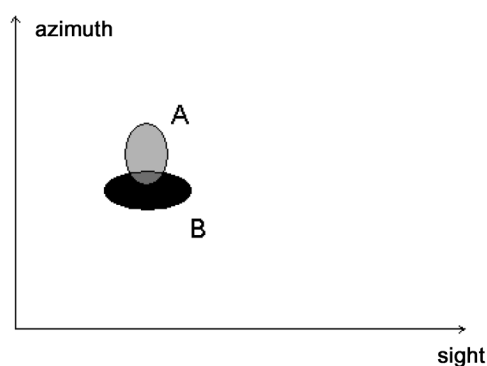


Fig. 13. Evaluation of the detection probability and the false alarm rate: A is a region considered by the expert as a "real" echo and B is a region segmented by the segmentation method.

- The original amplitude data are mapped in the mean–standard deviation plane.
- In this representation, echoes appear as horn-shaped structures whereas background pixels are closer to the origin (low mean and low standard deviation). Therefore, a double threshold (both in mean and in standard deviation)

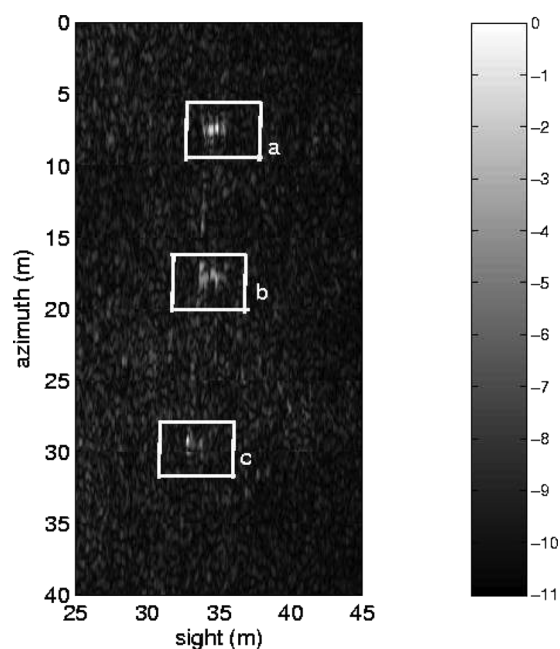


Fig. 14. SAS image containing three cylindrical mines (decibel scale, pixel size = 10 cm \times 10 cm, resolution: 20 cm \times 20 cm, antenna length: 80 cm).

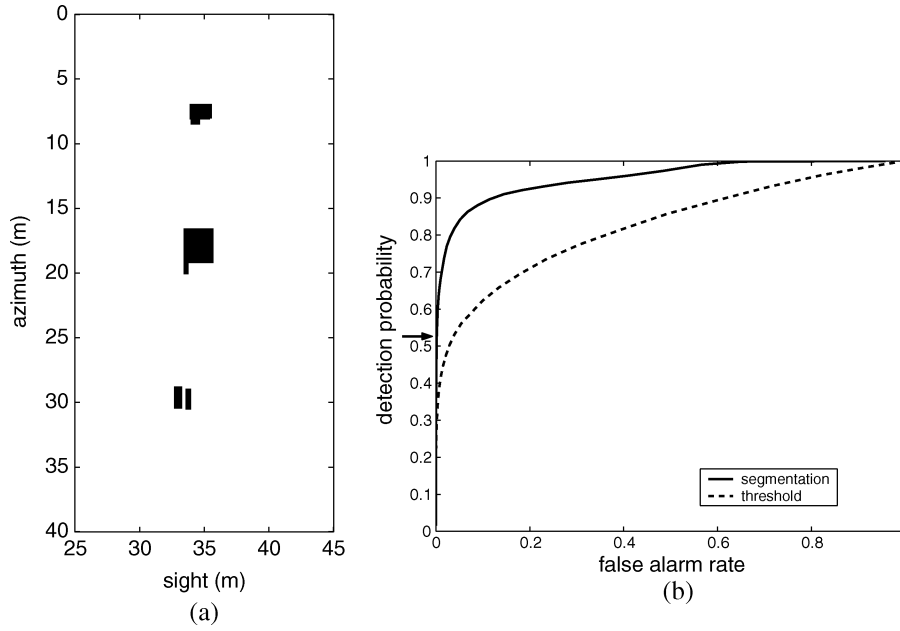


Fig. 15. Evaluation of the performances of the proposed segmentation method and a conventional amplitude threshold (image of Fig. 14, 50 realizations). (a) Binary ground truth (build by the expert). (b) ROC curves.

allows a separation of the echoes pixels from the background pixels. The threshold value in standard deviation is set, either manually or automatically as will be described in Section IV-B.

- Corresponding threshold value for the mean is obtained by multiplying the standard deviation threshold by the proportionality coefficient estimated for the Weibull law [see (7)].
- Application of both thresholds in the mean-standard deviation plane isolates corresponding echoes pixels in the original image.

Fig. 8(b) presents an original sonar image. Corresponding mean-standard deviation representation is presented in Fig. 8(a) where the dashed line represents the proportionality coefficient between mean and standard deviation (estimated with the Weibull law), and the solid lines feature the threshold values. Corresponding segmentation of the image is presented in Fig. 8(c): the echoes have been correctly set apart.

B. Automatic Setting of the Threshold Values Using Entropy Criterion

To automate the segmentation algorithm proposed in Section IV-A, we now propose a method to automatically set the standard deviation threshold value (the threshold value for the mean is then set accordingly). This is achieved in stepwise fashion by means of a progressive segmentation: the results obtained with decreasing standard deviation thresholds are computed. For each result, the spatial distribution of the segmented pixels is studied by computing corresponding entropies² with respect to the two axes, until a maximum value was reached. For each result, the histograms of the segmented

pixels along the X - and the Y -axis are computed and normalized (so that they sum to 1). See Fig. 10 for one example. Then, the entropy H_{axis} on each axis is computed by the following:

$$H_{\text{axis}} = - \sum_{i \in \mathcal{I}} p_{\text{axis}}(i) \log_2 p_{\text{axis}}(i) \quad (31)$$

with $p_{\text{axis}}(i)$ being the number of segmented pixels (after normalization) in the column (respectively, the line) number i , $\mathcal{I} = \{i = 1 \dots N_{\text{axis}} \text{ with } p_{\text{axis}}(i) \neq 0\}$, and N_{axis} being the number of columns (respectively, lines) of the original image. These entropies characterize the spreading of the segmented pixels in the SAS image: a uniform distribution of the segmented pixels over the image leads to high entropies, whereas very localized regions lead to small entropies.

As a consequence, a decrease of the threshold value (more pixels are segmented) leads to an increase of the entropy (segmented pixels tend to distribute over the whole image). However, this increase is not regular (see Fig. 11): for instance, two slope break points clearly appear in the entropy evolution along the azimuth axis and one appears for the sight axis (they are pointed out by arrows in Fig. 11). They correspond to the standard deviation threshold of about 6250 and 4000, respectively). For a better understanding of these irregularities, the segmentations corresponding to different threshold values are presented in Fig. 9: when the threshold progressively decreases, the first echo begins to be segmented; then, the second echo is segmented as well which explains the rapid increase of the entropy (break point 1). Finally, the random background reverberation is reached, with segmented pixels spread all over the image. This explains the sharp increase of entropy (break point 2). Note that with the two segmented echoes being parallel to the azimuth

²Entropy-based segmentation algorithms have already been proposed in the literature. For example, Pun used an entropy criterion, evaluated on the gray-level histogram [33], [34].

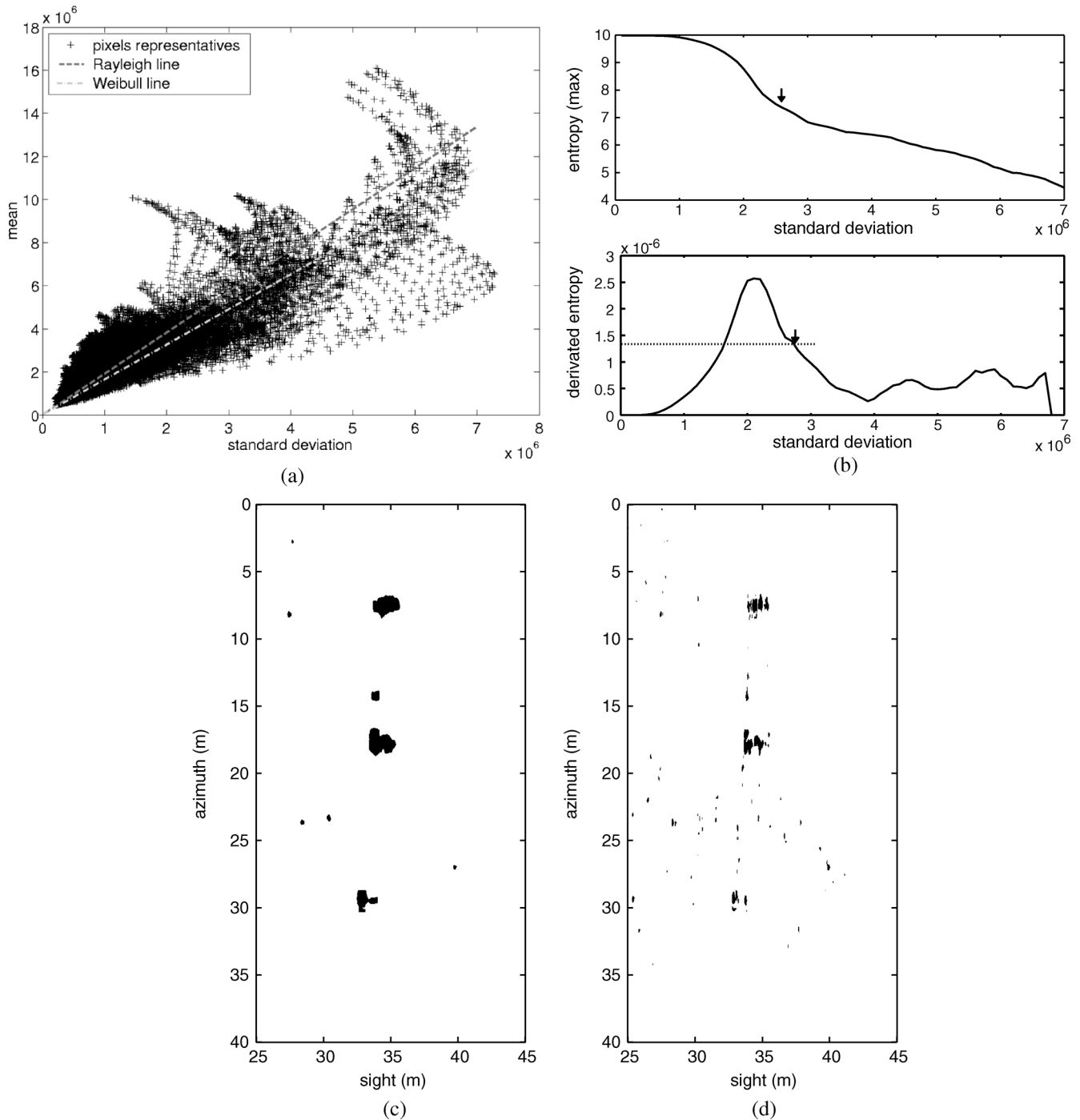


Fig. 16. Comparison between the proposed segmentation method and the conventional amplitude threshold on the SAS image of Fig. 14. (a) Mean–standard deviation representation. (b) Entropy profile (top) and its derivative (bottom). (c) Automatic segmentation std. – dev. = 2.70×10^6 , $p_{fa} = 0.0019$, $p_d = 0.5298$, and 9 regions. (d) Conventional amplitude threshold = 7.07×10^6 , $p_{fa} = 0.0018$, $p_d = 0.2949$, and 86 regions.

axis, the first slope breaking is only visible on the azimuth axis (the sight axis only “sees” one echo).

As a conclusion, the optimal segmentation, detecting both echoes with a maximal size but with no background element, is obtained with a threshold corresponding to the highest slope breaking (with a lower threshold, structures from the background are segmented generating false alarms in the system). This optimal threshold value is automatically detected from the derivative profile of the entropy. For this purpose, the

maximum³ of the two entropies defined previously is computed [see Fig. 12(a)]. The maximum of the derivative points out the highest slope breaking. However, to detect the real beginning of this slope breaking, the threshold corresponding to the half of this maximum is selected [see Fig. 12(b)].

The result obtained on the SAS image from this threshold is presented in Fig. 10: the two echoes are correctly segmented.

³Similar results are obtained with other combination operators (simple sum, quadratic sum, etc.).

C. Performance Evaluation

To assess the relevance of the proposed segmentation method, receiver operating characteristic (ROC) curves are computed on various real sonar data. The evolution of the detection probability versus the false alarm rate is plotted when the threshold value increases. These probabilities are evaluated using manually designed ground truth images. The set A of pixels assumed to actually belong to the echoes is determined by an expert. The result of the algorithm for a given threshold is the set B of segmented pixels (Fig. 13). With N_A being the number of pixels in A and $N_{A \cap B}$ being the number of pixels at the intersection of A and B , the detection probability p_d is estimated as

$$p_d = \frac{N_{A \cap B}}{N_A}. \quad (32)$$

The false alarm rate p_{fa} is estimated as

$$p_{fa} = \frac{N_{\bar{A} \cap B}}{N_{\bar{A}}} \quad (33)$$

with \bar{A} being the complementary set of A ($N_{\bar{A}} = N - N_A$ with N the size of the image). Note that, as is unusual in the mine hunting community, these parameters are evaluated at the pixel level, and not at the target level. Indeed, given the low number of targets in our images, the usual definitions would not be informative. Moreover, if we consider the detection of an echo by only one pixel, it would be useless for an expert who would not be able to distinguish it from a false alarm. The presented definitions would then be able to evaluate how each echo is detected (the size of each segmented region is taken into account).

Furthermore, the proposed method is compared with the conventional detection method consisting in directly thresholding the amplitude of the original data.

D. Results

In this section, we apply the proposed segmentation method to various sets of data. For each image, the proposed method is evaluated and compared with the conventional detector (amplitude threshold) with corresponding ROC curves.

The first data set represents a region of $40 \times 20 \text{ m}^2$ of the seabed with a pixel size of about 4 cm in both directions. It is presented in [35] and [36]. It contains three cylindrical underwater mines whose corresponding echoes are indicated with boxes in Fig. 14: (a) the mine is lying on the seabed; (b) the mine is partially buried (about 2/3); and (c) the mine is completely buried in the seafloor. In this case, there is no shadow cast on the seafloor. This underlines the interest for a mine detection algorithm solely based on the echoes.

Fig. 16(a) presents the mean-standard deviation representation of the image with the estimated linear approximations. Fig. 16(b) presents the derivative entropy profiles with the small arrow indicating the threshold values automatically computed for the standard deviation (we recall that the threshold value for the mean is then obtained using the estimated Weibull proportionality coefficient).

Fig. 15(a) presents the binary ground truth designed by an expert. Fig. 15(b) presents the ROC curves obtained with the

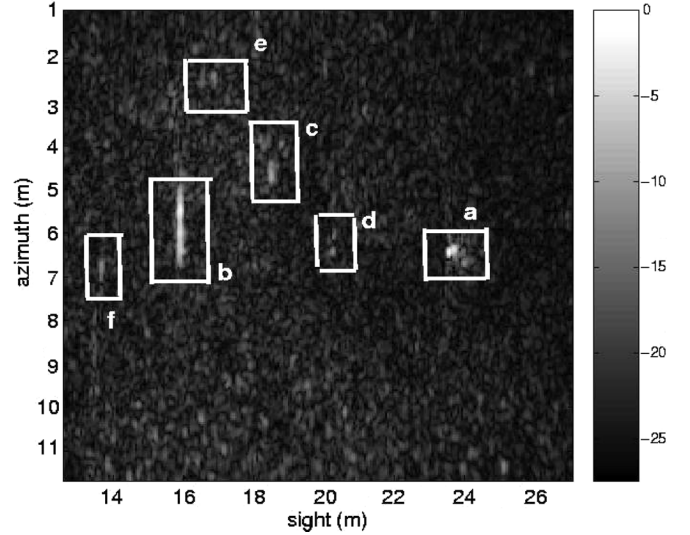


Fig. 17. SAS image containing several buried and proud objects (decibel scale, pixel size = 4 cm \times 4 cm, resolution: 10 cm \times 10 cm, antenna length: 40 cm).

proposed method (solid line) which clearly outperforms the conventional threshold (dashed line). The small horizontal arrow indicates the position corresponding to the automatic optimal threshold. The result of the proposed algorithm (i.e., the segmentation obtained from this optimal value) is presented in Fig. 16(c). The three sought echoes are correctly detected and there are a few false alarms. The results obtained with the conventional amplitude threshold are presented in Fig. 16(d): there are clearly more false alarms and the echoes are less visible. This visual inspection confirms the results of the ROC curves.

Fig. 17 presents another data set containing proud and buried objects (indicated by small boxes). There is one underwater mine lying on the seabed on the right (a), and several buried mines (b,d, and e). There is also a buried rock (c) and an unidentified object (f) which are hardly visible. This image represents a seabed region of about $12 \times 10 \text{ m}^2$, with a resolution of about 10 cm in both directions.

Fig. 19(a) presents the mean-standard deviation representation of the image with the estimated linear approximations. Fig. 19(b) presents the derivative entropy profiles with the small arrow indicating the automatically computed threshold value for the standard deviation.

Fig. 18(a) presents the binary ground truth designed by an expert. Fig. 18(b) presents the ROC curves obtained with the proposed method (solid line) which clearly outperforms again the conventional threshold (dashed line). The results obtained with the proposed algorithm and the conventional threshold are presented in Fig. 19(c) and (d), respectively. The same comment can be made: the proposed algorithm correctly detect the objects of interest with less false alarms than the conventional method.

V. CONCLUSION

In this paper, we proposed an echo detection method with application to SAS images. A study of the statistical properties

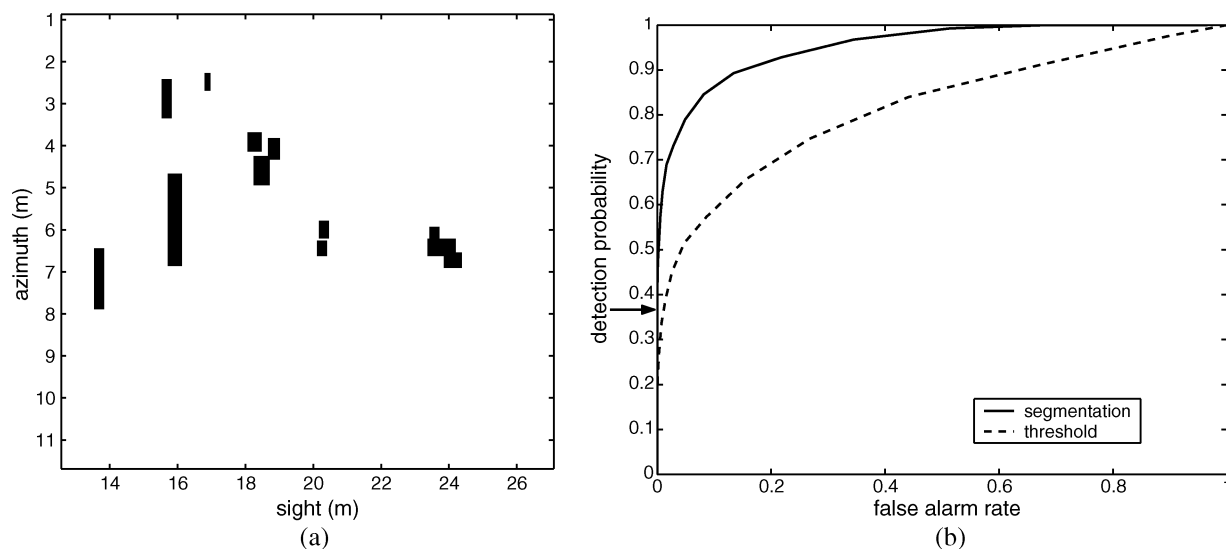


Fig. 18. Evaluation of the performances of the proposed segmentation method and a conventional amplitude threshold (image of Fig. 17, 50 realizations). (a) Binary ground truth (built by the expert). (b) ROC curves.

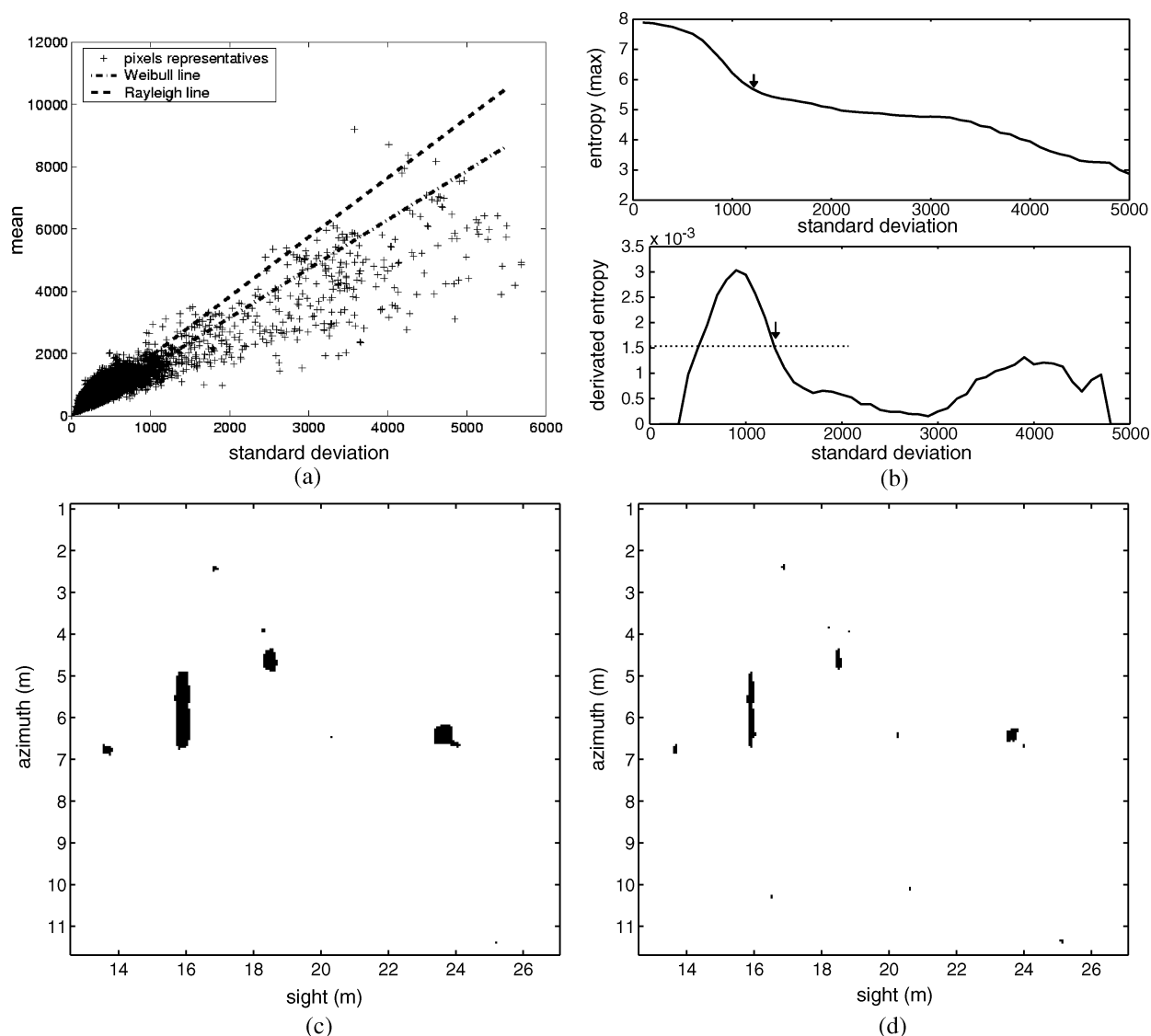


Fig. 19. Comparison between the proposed segmentation method and the conventional amplitude threshold on the SAS image of Fig. 17. (a) Mean-standard deviation representation. (b) Entropy profile (top) and its derivative (bottom). (c) Automatic segmentation std. - dev. = 1200, $p_{fa} = 0.10 \cdot 10^{-4}$, $p_d = 0.381$, and 8 regions. (d) Conventional amplitude threshold = 3200, $p_{fa} = 1.28 \cdot 10^{-4}$, $p_d = 0.160$, and 12 regions.

of data was first presented and various models of amplitude distribution have been discussed (e.g., Rayleigh distribution, Weibull distribution, and K -distribution), with an emphasis on Weibull distribution as the best tradeoff for high-resolution SAS data. All these distributions share a common property: the first and the second statistical moments are proportional. Focusing on these two first moments, we propose to map the original SAS image onto the mean-standard deviation plane. As a matter of fact, with this representation, the echoes can be separated from the reverberation background using a double threshold (in the standard deviation and in the mean direction, respectively—these two thresholds being linked by the proportionality relation). Furthermore, the setting of these values can be automated with the help of an entropy criterion that characterizes how the segmented pixels spread over the image. The method is simple. It does not require any *a priori* information (apart from not restrictive hypothesis such as the approximative mean spatial extension of the echoes) nor any gain correction between the beginning and the end of the scene on the SAS image.

The method has been tested and validated on various SAS data with different resolutions. Quantitative evaluation and comparison with a simple conventional method have been positively achieved by means of ROC curves.

From an operational point of view, the proposed method does not provide a perfect detection of underwater mines. Though most of the few remaining false alarms can easily be removed by some simple image processing algorithm (median filter, etc.), some detected echoes may be spurious (rocks). Therefore, the method should be considered as a support for the user, selecting some regions of interest in the picture, the final classification (mine/not mine) remaining his/her call. However, the method is fairly reliable (all the actual mines, including the buried ones, are always detected and there are only a few false alarms) and the performances have been assessed by ROC curves.

Further developments include the use of higher order statistics [37], [38] and data fusion [39]–[41] to further decrease the false alarm rate while preserving the good detection performances.

Finally, one should also underline that the proposed algorithm could be used in a variety of sonar applications with different resolutions or configurations.

A clear limitation of all the detection methods based on statistics is the lack of accurate physical model. Future detection algorithms will surely include more precise physical considerations. For instance, modeling the wave propagation and the actual generation of the echoes should lead to a refined model, differing from a simple deterministic element with a constant amplitude. This requires the injection of precise knowledge about the transmitter and the channel of propagation. A more physical approach could help further improving the detection performances, for instance, by discriminating actual mines from rocks, thus further reducing the false alarm rate.

ACKNOWLEDGMENT

The authors would like to thank the Groupe d'Etudes Sous-Marines de l'Atlantique (DGA/DET/GESMA, Brest Armées, France) and Nederlandse Organisatie voor Toegepast-Natuurwetenschappelijk Onderzoek (TNO) Defence, Security and

Safety (The Netherlands) for providing SAS data in this work supported by GESMA.

REFERENCES

- [1] U.S. Department of the Navy, "The Navy unmanned undersea vehicle (UUV) master plan," Apr. 2000 [Online]. Available: <http://www.npt.nuwc.navy.mil/UUV>
- [2] D. Attali, J. Chanussot, R. Aresté, and S. Guyonic, "3D snakes for the segmentation of buried mines in 3D acoustical images," in *Proc. IEEE OCEANS Eur. Conf.*, Brest, France, Jun. 2005, pp. 442–446.
- [3] P. T. Gough and D. W. Hawkins, "A short history of synthetic aperture sonar," in *Proc. IEEE Int. Geosci. Remote Sens. Symp.*, Seattle, WA, Jul. 1998, pp. 618–620.
- [4] M. P. Hayes and P. T. Gough, "Synthetic aperture sonar: A maturing discipline," in *Proc. 7th Eur. Conf. Underwater Acoust.*, Delft, The Netherlands, Jul. 2004, pp. 1101–1106.
- [5] M. P. Hayes and P. T. Gough, "Using synthetic aperture sonar for mine detection," in *Proc. Austral.-Amer. Joint Conf. Technol. Mines Mine Countermeas. Syst.*, Sydney, Australia, Jul. 1999, pp. 1.1–1.10.
- [6] M. Pinto, A. Belletini, L. Wang, and P. Munk, "High and low frequency synthetic aperture sonar for AUV based mine hunting," in *Proc. 7th Eur. Conf. Underwater Acoust.*, Delft, The Netherlands, Jul. 2004, pp. 1145–1150.
- [7] J. G. Abbot and F. L. Thurstone, "Acoustic speckle: Theory and experimental analysis," *Ultrason. Imag.*, no. 1, pp. 303–324, 1979.
- [8] F. Maussang, J. Chanussot, S. C. Visan, and M. Amate, "Adaptive anisotropic diffusion for speckle filtering in SAS imagery," in *Proc. IEEE OCEANS Eur. Conf.*, Brest, France, Jun. 2005, pp. 305–309.
- [9] J. Chanussot, A. Hétet, G. Le Merrer, and E. Tireau, "Multispectral decomposition of synthetic aperture sonar images for speckle reduction," in *Proc. 6th Eur. Conf. Underwater Acoust.*, Gdansk, Poland, Jun. 2002, pp. 269–274.
- [10] J. Chanussot, F. Maussang, and A. Hétet, "Scalar image processing filters for speckle reduction on synthetic aperture sonar images," in *Proc. MTS/IEEE OCEANS Conf.*, Biloxi, MS, Oct. 2002, pp. 2294–2301.
- [11] J. S. Lee, "Speckle analysis and smoothing of synthetic aperture radar images," *Comput. Graphics Image Process.*, vol. 17, pp. 24–31, 1981.
- [12] D. Coltuc and R. Radescu, "On the homomorphic filtering by Chanell's summation," in *Proc. IEEE Int. Geosci. Remote Sens. Symp.*, Toronto, ON, Canada, Jun. 2002, vol. 4, pp. 2456–2458.
- [13] S. Batman and J. Goutsias, "Robust morphological detection of sea mines in side-scan sonar images," in *Proc. SPIE Detection & Remediation Technol. Mines Minelike Targets VI*, Orlando, FL, Apr. 2001, vol. 4394, pp. 1103–1115.
- [14] C. Collet, P. Thourel, M. Mignotte, P. Pérez, and P. Bouthemy, "Segmentation markovienne hiérarchique multimodèle d'images sonar haute résolution," *Traitement du Signal*, vol. 15, no. 3, pp. 231–250, Oct. 1998.
- [15] M. Mignotte, C. Collet, P. Pérez, and P. Bouthemy, "Unsupervised Markovian segmentation of sonar images," in *Proc. IEEE Int. Conf. Acoust. Speech Signal Process.*, Munchen, Germany, May 1997, vol. 4, pp. 781–785.
- [16] M. Mignotte, C. Collet, P. Pérez, and P. Bouthemy, "Three-class Markovian segmentation of high-resolution sonar images," *Comput. Vis. Image Understanding*, vol. 76, no. 3, pp. 191–204, Dec. 1999.
- [17] M. Mignotte, C. Collet, P. Pérez, and P. Bouthemy, "Hybrid genetic optimization and statistical model-based approach for the classification of shadow shapes in sonar imagery," *IEEE Trans. Pattern Anal. Mach. Intell.*, vol. 22, no. 2, pp. 129–141, Feb. 2000.
- [18] S. Reed, Y. Petillot, and J. Bell, "An automatic approach to the detection and extraction of mine features in sidescan sonar," *IEEE J. Ocean. Eng.*, vol. 28, no. 1, pp. 90–105, Jan. 2003.
- [19] T. Aridgides, M. Fernández, and G. Dobeck, "Side scan sonar imagery fusion for sea mine detection and classification in very shallow water," in *Proc. SPIE Detection Remediation Technol. Mines Minelike Targets VI*, Orlando, FL, Apr. 2001, vol. 4394, pp. 1123–1134.
- [20] S. W. Perry and L. Guan, "Pulse-length-tolerant features and detectors for sector-scan sonar imagery," *IEEE J. Ocean. Eng.*, vol. 29, no. 1, pp. 138–156, Jan. 2004.
- [21] J. C. Hyland and G. J. Dobeck, "Sea mine detection and classification using side-looking sonar," in *Proc. SPIE Detection Technol. Mines Minelike Targets*, Orlando, FL, Apr. 1995, vol. 2496, pp. 442–453.
- [22] A. P. Hétet, "Evaluation of specific aspects of synthetic aperture sonar, by conducting at sea experiments with a rail, in the frame of mine hunting systems design," in *Proc. 5th Eur. Conf. Underwater Acoust.*, Lyon, France, Jul. 2000, pp. 439–444.
- [23] F. Schmitt, M. Mignotte, C. Collet, and P. Thourel, "Estimation of noise parameters on sonar images," in *Proc. SPIE Conf. Signal Image Process.*, Denver, CO, Aug. 1996, vol. 2823, pp. 1–12.
- [24] M. Gu and D. A. Abraham, "Using McDaniel's model to represent non-Rayleigh reverberation," *IEEE J. Ocean. Eng.*, vol. 26, no. 3, pp. 348–357, Jul. 2001.

- [25] A. Hanssen, J. Kongsli, R. E. Hansen, and S. Chapman, "Statistics of synthetic aperture sonar images," in *Proc. MTS/IEEE OCEANS Conf.*, San Diego, CA, Sep. 2003, pp. 2635–2640.
- [26] G. Saporta, *Probabilités, analyse des données et statistique*. Paris, France: Technip, 1990.
- [27] I. R. Joughin, D. B. Percival, and D. P. Winebrenner, "Maximum likelihood estimator of K distribution parameters for SAR data," *IEEE Trans. Geosci. Remote Sens.*, vol. 31, no. 5, pp. 989–999, Sep. 1993.
- [28] F. Maussang, J. Chanussot, C. Hory, and A. Hétet, "Synthetic aperture sonar imagery: Towards a classification of underwater mines in the mean-standard deviation plane," in *Proc. Phys. Signal Image Process.*, Grenoble, France, Jan. 2003, pp. 137–140.
- [29] F. Maussang, J. Chanussot, and A. Hétet, "Automated segmentation of SAS images using the mean-standard deviation plane for the detection of underwater mines," in *Proc. MTS/IEEE OCEANS Conf.*, San Diego, CA, Sep. 2003, pp. 2155–2160.
- [30] C. Hory, N. Martin, and A. Chehikian, "Spectrogram segmentation by means of statistical features for non-stationary signal interpretation," *IEEE Trans. Signal Process.*, vol. 50, no. 12, pp. 2915–2925, Dec. 2002.
- [31] G. Ginolhac, J. Chanussot, and C. Hory, "Morphological and statistical approaches to improve detection in the presence of reverberation," *IEEE J. Ocean. Eng.*, vol. 30, no. 4, pp. 881–899, Oct. 2005.
- [32] M. G. Kendall and A. Stuart, *The Advanced Theory of Statistics*, 2nd ed. London, U.K.: Griffin, 1963, vol. 1.
- [33] T. Pun, "A new method for grey-level picture thresholding using the entropy of the histogram," *Signal Process.*, vol. 2, no. 3, pp. 223–237, Jul. 1980.
- [34] T. Pun, "Entropic thresholding, a new approach," *Comput. Graphics Image Process.*, vol. 16, pp. 210–239, 1981.
- [35] A. Hétet, M. Amate, B. Zerr, M. Legris, R. Bellec, J. C. Sabel, and J. Groen, "SAS processing results for the detection of buried objects with a ship-mounted sonar," in *Proc. 7th Eur. Conf. Underwater Acoust.*, Delft, The Netherlands, Jul. 2004, pp. 1127–1132.
- [36] J. C. Sabel, J. Groen, M. E. G. D. Colin, B. A. J. Quesson, A. Hétet, B. Zerr, M. Brussieux, and M. Legris, "Experiments with a ship-mounted low frequency SAS for the detection of buried objects," in *Proc. 7th Eur. Conf. Underwater Acoust.*, Delft, The Netherlands, Jul. 2004, pp. 1133–1138.
- [37] F. Maussang, J. Chanussot, and A. Hétet, "On the use of higher order statistics in SAS imagery," in *Proc. Int. Conf. Acoust. Speech Signal Process.*, Montreal, QC, Canada, May 2004, pp. 269–272.
- [38] F. Maussang, J. Chanussot, A. Hétet, and M. Amate, "Higher order statistics for the detection of small objects in a noisy background, application on sonar imaging," *EURASIP J. Adv. Signal Process.*, vol. 2007, Jan. 2007, doi:10.1155/2007/47039, Article ID 47039.
- [39] F. Maussang, M. Rombaut, J. Chanussot, and A. Hétet, "Fusion of local statistical detectors in SAS imagery identification," in *Proc. IEEE OCEANS Eur. Conf.*, Brest, France, Jun. 2005, pp. 299–304.
- [40] G. Ginolhac, J. Chanussot, and C. Pichat, "Fusion algorithms from a sonar images sequence for detection," in *Proc. 6th Eur. Conf. Underwater Acoust.*, Gdansk, Poland, Jun. 2002, pp. 711–716.
- [41] J. Chanussot, G. Mauris, and P. Lambert, "Fuzzy fusion techniques for linear features detection in multi-temporal SAR images," *IEEE Trans. Geosci. Remote Sens.*, vol. 37, no. 3, pp. 1292–1305, May 1999.



Frédéric Maussang graduated in electrical engineering from the Grenoble Institute of Technology (INP Grenoble), France, in 2002, and received the Ph.D. degree from the University of Grenoble 1, Grenoble, France, in 2005. He prepared his Ph.D. degree at the Signals and Images Laboratory (LIS—GIPSA Lab), Grenoble, France, on image processing and data fusion for detection in acoustical imaging.

Since September 2006, he has been teaching electronics at the University of Paris X and he is working in the research team GEA (Applied Electromagnetism Group). His research interests are multistatic radar imagery and ground target detection.

Dr. Maussang is a Reviewer for the IEEE TRANSACTIONS ON IMAGE PROCESSING and the IEEE TRANSACTIONS ON GEOSCIENCE AND REMOTE SENSING.



Jocelyn Chanussot (SM'04) graduated in electrical engineering from the Grenoble Institute of Technology (INP Grenoble), France, in 1995, and he received the Ph.D. degree from the Savoie University, Annecy, France, in 1998.

He was with the Automatics and Industrial Micro-Computer Science Laboratory (LAMII). In 1999, he worked at the Geography Imagery Perception laboratory (GIP) for the Délégation Générale de l'Armement (DGA—French National Defense Department). Since 1999, he has been with INP Grenoble as an Assistant Professor (1999–2005), an Associate Professor (2005–2007) and a Professor (2007–present) of signal and image processing. He is conducting his research at the Grenoble Images Speech Signals and Automatics (GIPSA-Lab, Grenoble, France). He is especially involved in the team working on geophysical and underwater acoustical signal and image processing. His research interests include multicomponent image processing, nonlinear filtering, remote sensing, data fusion, and their applications to natural real bidimensional data (seismic data, sonar images, optical remote sensing).

Prof. Chanussot is an Associate Editor for the IEEE TRANSACTIONS ON GEOSCIENCE AND REMOTE SENSING and for *Pattern Recognition*. He is the Co-Chair of the GRS Data fusion Technical Committee and a Member of the Machine Learning for Signal Processing Technical Committee of the IEEE Signal Processing Society.



Alain Hétet graduated from the Ecole Nationale Supérieure d'Ingénieurs d'Etudes en Techniques de l'Armement (ENSIETA), Brest, France, and received the Ph.D. degree in acoustics from the University of Paris VI, Paris, France.

Currently, he is working as an Underwater Mine Warfare Expert in the Groupe d'Etudes Sous-Marines de l'Atlantique (DGA/GESMA), Brest, France. He is acting as a Scientist and a Project Leader in the area of advanced mine hunting sonar designs. His interests include all aspects of synthetic aperture sonar, proud and buried mines detection and classification. He made some experimental and data analysis work under international collaborations. His past work includes acting in the Direction des Constructions Navales (DCN) as an engineer in the design, integration and trials of systems during shipbuilding phases.



Maud Amate graduated from the Ecole Nationale Supérieure d'Ingénieurs d'Etudes en Techniques de l'Armement (ENSIETA), Brest, France, and received the M.Sc. degree in digital signal and image processing from Cranfield University, United Kingdom.

She has been working as an Underwater Mine Warfare Expert in the Groupe d'Etudes Sous-Marines de l'Atlantique (DGA/DET/GESMA), Brest, France, since 2003. Her interests include SAS systems.